S & M 4161

Multi-temporal Interferometric Synthetic Aperture Radar for Monitoring and Application Analysis of Highway Slope

Guoshi Liu, ¹ Wanji Zheng, ^{2*} You Yu, ³ Xiaohong Chen, ⁴ Ciguo Mo, ⁴ and Min Lv¹

¹Key Laboratory of Green Construction and Intelligent Monitoring in Southwestern Hunan for Regular Higher Educational Institutions of Hunan Province, Shaoyang University, Shaoyang 422000, China
 ²School of Geosciences and Info-physics, Central South University, Changsha 410083, China
 ³Hunan Province Geological Disaster Survey and Monitoring Institute, Changsha 410014, China
 ⁴Geologic and Geophysical Engineering Exploration Institute of Guangdong Province, Guangzhou 510000, China

(Received December 26, 2024; accepted September 4, 2025)

Keywords: highway slope, deformation, TCP-InSAR, Fengkai

Surface deformation is as a crucial precursor indicator in the evaluation of highway slope instability. Therefore, the systematic monitoring of deformations is of paramount significance for a comprehensive assessment of highway slope stability. In this work, we employed Interferometric Synthetic Aperture Radar (InSAR) technology to monitor deformations in small-scale highway slopes, specifically focusing on the left slope of the K2+500 section within the Guangkun Expressway Fengkai connection line in Guangdong Province. Deformation monitoring results were derived from C-band Sentinel-1A and L-band ALOS-2 PALSAR2 images. The analysis revealed that acquiring effective deformation phases on the slope using medium-resolution Sentinel-1A images is challenging, primarily owing to the limited geometry size of the slope and the coherence maintenance capability of the C-band. In contrast, the deformation characteristics during the period from October 28, 2017 to April 27, 2019 were effectively revealed through the TCP-InSAR processing of five high-resolution L-band ALOS-2 PALSAR2 images. The InSAR results indicated a prominent deformation zone in the northeastern corner of the slope, exhibiting a maximum deformation velocity of approximately -60 mm/yr. The ongoing deformation process has also affected the secondary berm of the slope, emphasizing the need for the highway management department to focus on preventing and controlling this hidden danger point. Additionally, an obvious deformation area was detected in the southwest trailing edge of the slope. Time series analysis showed that the deformation area accelerated only from October 28, 2017 to April 28, 2018, and then tended to stabilize. Owing to the low temporal resolution of ALOS-2 PALSAR2 images, the underlying mechanism driving this acceleration remains undisclosed. Nevertheless, vigilance towards this potential hazard point by highway management authorities is warranted. In this work, ALOS-2 PALSAR2 data with low temporal resolution were utilized to monitor the deformation characteristics of the slope, yielding some notable results. Building upon this foundation, we discuss the potential applications of L-band LT-1 and NISAR data, anticipating a significant enhancement in the capability of InSAR technology to monitor the fine deformation of small-scale highway slopes.

*Corresponding author: e-mail: <u>zwanji@foxmail.com</u> https://doi.org/10.18494/SAM5523

1. Introduction

In recent decades, China has significantly increased its investment in transportation infrastructure construction, (1) particularly through the implementation of the transportation power strategy. As a result, China now boasts the highest total mileage of highways globally.⁽²⁾ The convenient highway network has brought significant social and economic benefits to urban development, logistics transportation, and daily travel in remote areas. However, the presence of unstable geological conditions and limited construction budgets and timeframes, among other factors, has resulted in a proliferation of steep slopes along highways. (1) These slopes are highly susceptible to deformation owing to internal and external influences such as heavy rainfall and gravity. (3,4) The deformation of highway slopes serves as the most direct indicator of their stability. Despite their clear importance, incidents of slope damage on highways occur frequently, attributable to inadequate identification and insufficient preventive measures. (1,5,6) Note that noting that the collapse of the Meida Expressway on May 1, 2024, which resulted in 48 fatalities, has raised significant public and academic concern regarding the safety of highway slopes. (7) Consequently, it is imperative to implement the high-precision monitoring of highway slope deformations to ensure safe operations and prevent potential secondary disasters during remedial actions. Conventional geodetic methods, such as leveling and GNSS measurements, are characterized by being time-consuming and labor-intensive and possessing limited spatial resolution.⁽⁸⁾ Interferometric synthetic aperture radar (InSAR) is an advanced Earth observation technology developed in recent decades that offers the advantages of all-weather capability, high precision, and spatial continuity. Additionally, it enables the utilization of satellite archive images for historical deformation analysis. Consequently, InSAR has become a crucial method for monitoring deformation phenomena in various contexts, such as earthquakes, (9) volcanoes, (10) glaciers,(11) dams,(12,13) and landslides.(14-16)

In its initial stages, the application of InSAR technology in highway slope monitoring faced limitations owing to the scarcity of SAR satellites in orbit and its relatively low spatio-temporal resolution. However, in recent years, we have witnessed a significant improvement in the operation of high-resolution SAR satellite sensor platforms such as ALOS and TerraSAR-X, enriching the availability of historical archive data. Furthermore, the launch of ESA's Sentinel-1 A/B SAR satellites, coupled with an open access strategy, has substantially lowered the data threshold for users. This development has created favorable conditions for researchers, enabling them to effectively leverage InSAR technology in highway slope monitoring. The evidence of the enhanced utility of InSAR technology is reflected in various studies. For instance, Gong et al. identified eight potential frozen debris lobes along the northern Alaska Dalton Highway by analyzing ERS1 and ALOS-1 PARSAR data. (17) Su et al. successfully detected 762 potential landslides along the China-Pakistan Karakoram Highway, employing the SBAS processing of Sentinel-1A Ascending data. (18) In the G213 highway in Wenchuan County, China, Zhang et al. applied the Stacking-InSAR method based on Sentinel-1A data to identify 72 highway slopes with significant deformation. (19) This study highlights the capability of InSAR technology, utilizing Sentinel-1 data, to detect steep active slopes along typical mountainous highways. Moreover, Zocchi et al. evaluated slope instability along transportation corridors using UAV and

InSAR methods.⁽²⁰⁾ They concluded that C-band Sentinel data-based InSAR technology is well suited for detecting the deformation of large-scale highway slopes. These collective studies underscore the increasing effectiveness and versatility of InSAR technology in monitoring and assessing the stability of highway slopes.

However, these previous studies have focused on identifying unstable slopes with deformation near highways, and there are few cases in which InSAR technology is used to study the detailed characteristics of highway slope deformation. On the basis of Sentinel-1 A data and StaMPS, Zhang et al. obtained the deformation details of the Lashagou landslide near the G310 highway in Gansu Province, China, and revealed the temporal and spatial evolution and failure mode of the landslide group. (21) The geometric size of the landslide is about 460000 m², which belongs to the large-scale landslide group. However, in China, the majority of destructive events occur on small-scale slopes along mountainous highways. These slopes are widely distributed and numerous, yet their deformation monitoring is often overlooked owing to the high cost of ground monitoring methods. (8,22) Possibly owing to resolution constraints—for example, Sentinel-1 A/B provides a spatial resolution of 2.3 × 13.9 m²—few InSAR studies have focused on the detailed deformation of small highway slopes. Therefore, it would be meaningful to employ InSAR technology to monitor small-scale steep mountainous highway slopes. The left section of the K2+458-640 cutting slope of the Fengkai connector line on the Guangkun Expressway was selected as the study area in this work, with deformation details monitored using ascending data from ALOS-2 PARSAR2 and Sentinel-1A. On the basis of these monitoring results, we discuss the potential application of future high-spatiotemporal-resolution L-band SAR satellite images in small-scale steep highway slope monitoring.

The structure of this paper is as follows: In Sect. 2, we provide a summary of the geographical scene of the study area and outline the SAR data employed in this investigation. In Sect. 3, we describe in detail the InSAR time-series processing method. In Sect. 4, we present the InSAR results and comprehensively discuss the deformation characteristics observed in the slope. The conclusions drawn from our work are presented in Sect. 5.

2. Study Site and Dataset

2.1 Study site

The Hekou to Pingtai Expressway is situated in Yunfu City, Guangdong Province, China. It forms part of China's national expressway network known as the Guangkun Expressway (code name G80), which was fully completed and opened for traffic on June 30, 2010. The Fengkai connecting line serves as a vital trunk highway linking Fengkai County with the Yunan toll station of the G80 Expressway. This highway has been constructed according to secondary highway standards. Its operation shortens the distance from Fengkai County to the expressway to 15 km, eliminating its historical lack of an expressway connection and making a substantial contribution to local economic development. Despite these benefits, the highway traverses a mountainous terrain in western Guangdong, leading to steep slopes resulting from cost constraints during construction. Notably, the left section of the K2+458–640 cutting slope

(depicted in Fig. 1) exemplifies this topographical challenge. Formed during the highway's construction [as illustrated in Fig. 1(b)], this slope experienced a slip event during its operational phase. In response to this, the highway management department reinforced the slope in March 2013. To ensure the safety of the highway operation and enhance slope stability, a three-tiered design was implemented during construction. The tiers, with respective heights of 10, 10, and 12 m, featured a slope ratio of 1:1. Grass was established on the slope beneath the arch to mitigate surface erosion caused by rainfall. Moreover, water cut ditches were established at the top of each tier to mitigate soil softening caused by heavy rainfall infiltration, while drainage ditches were strategically placed at the foot of each level. By late 2013, the slope treatment construction was completed, as depicted in Fig. 1(c) and outlined by red dotted lines.

However, in 2016, a significant landslide occurred on the slope, introducing a substantial and immediate threat to the secure operation of the highway, as indicated by the dotted line in Fig. 2(a). In response, the highway management department devised and executed a reinforcement

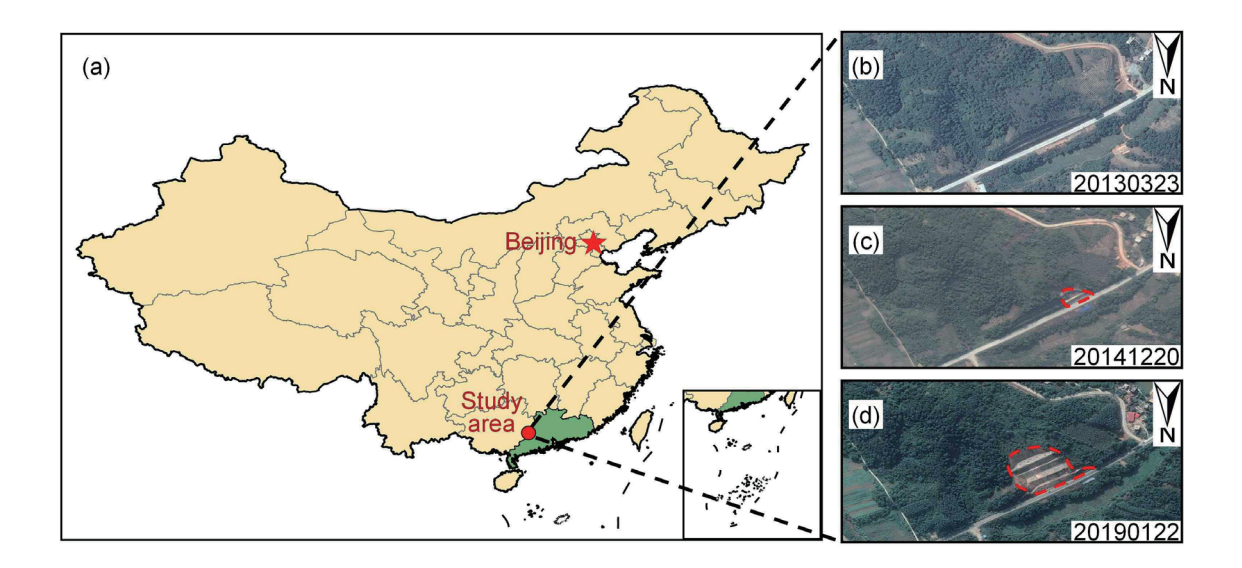


Fig. 1. (Color online) (a) Location of study area in China. (b) Preconstruction state of a highway slope. (c) Postconstruction view of the highway slope, with the red dotted line representing the reinforced area. (d) Scene after the reinforcement of the highway slope.

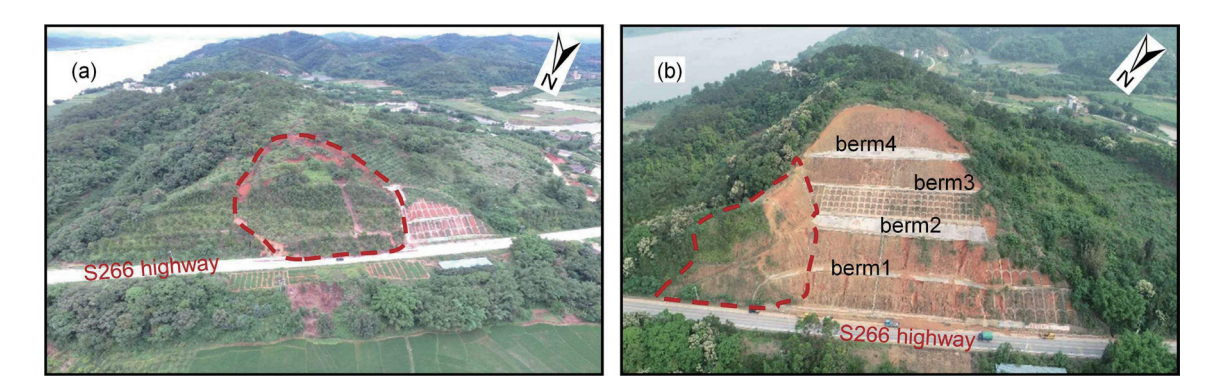


Fig. 2. (Color online) (a) Scenario of highway slope sliding. (b) UAV imagery depicting the scene after the reinforcement of the highway slope, with the red dotted line representing the unreinforced area.

plan that combined brush side load reduction with a footwall retaining wall scheme. This construction plan entailed an elevation in the slope rate from three to five levels, incorporating concrete prefabricated footwalls, concrete water stops, and platform water stops. Furthermore, as part of the reinforcement strategy, inclined drainage holes, each measuring 20 m in length, were strategically installed 50 cm above the first and third slopes to facilitate efficient water drainage. The slope reinforcement project commenced in June 2016 and achieved completion by March 2017. A visual representation of the impact of these measures is presented through a comparison of UAV aerial images captured before and after the reinforcement in Fig. 2.

However, following the completion of the treatment project, we observed persistent and significant deformation phenomena on the slope. Specifically, beyond the K2+590-+634 segment, other sections of the slope's foot retaining wall displayed notable outward deformations, with on-site dislocations at the top measuring 2–3.5 cm. The first and second slope surfaces exhibited more severe conditions, characterized by individual sections with gullies as deep as 2 m. The erosion and destruction of the slope led to the formation of hollowed-out or collapsed areas on the platform, resulting in cavities. Moreover, there is substantial silt accumulation in the drainage side ditch at the base of the slope. Additionally, the arch skeleton has suffered serious damage.

To mitigate the potential slope-induced hazards and ensure the safe operation of the highway, it is imperative to conduct a comprehensive monitoring program for slope deformation, aiming at obtaining a detailed understanding of its spatial distribution and temporal evolution. Considering the limited geometric dimensions of the slope (length less than 150 m and width less than 120 m) as well as the high cost associated with conventional ground-based monitoring techniques, we advocate the utilization of InSAR technology for monitoring small-scale highway slopes.

2.2 SAR data

The slope remediation began in 2013 at the earliest. Since then, the currently operational SAR satellite platforms encompass TerraSAR-X, Cosmo-Skymed, Sentinel-1A/B, Radarsat-2, and ALOS-2 PALSAR2. The results of the query conducted on the official data website are illustrated in Fig. 3.

The query results showed that TerraSAR-X lacks archival data in ultrahigh-resolution modes such as Spotlight, High-Resolution Spotlight, and Staring for the designated study area. The available StripMap mode data comprises a total of 12 scenes, captured monthly from August 2018 to June 7, 2019. However, the coverage area of the TerraSAR-X StripMap mode data appears relatively marginal, likely inadequately encompassing the study area. Consequently, it may not be suitable for application in this case. Cosmo—Skymed is also a high-resolution SAR satellite that was considered; however, only one scene archive data covering the study area since 2013 was found, which cannot be used for interferometric processing using InSAR technology to extract deformation features.

The Sentinel-1A/B satellite constellation, launched by the European Space Agency (ESA) in 2014 for earth observation tasks, operates in the C band with a revisit cycle of 12 days and a

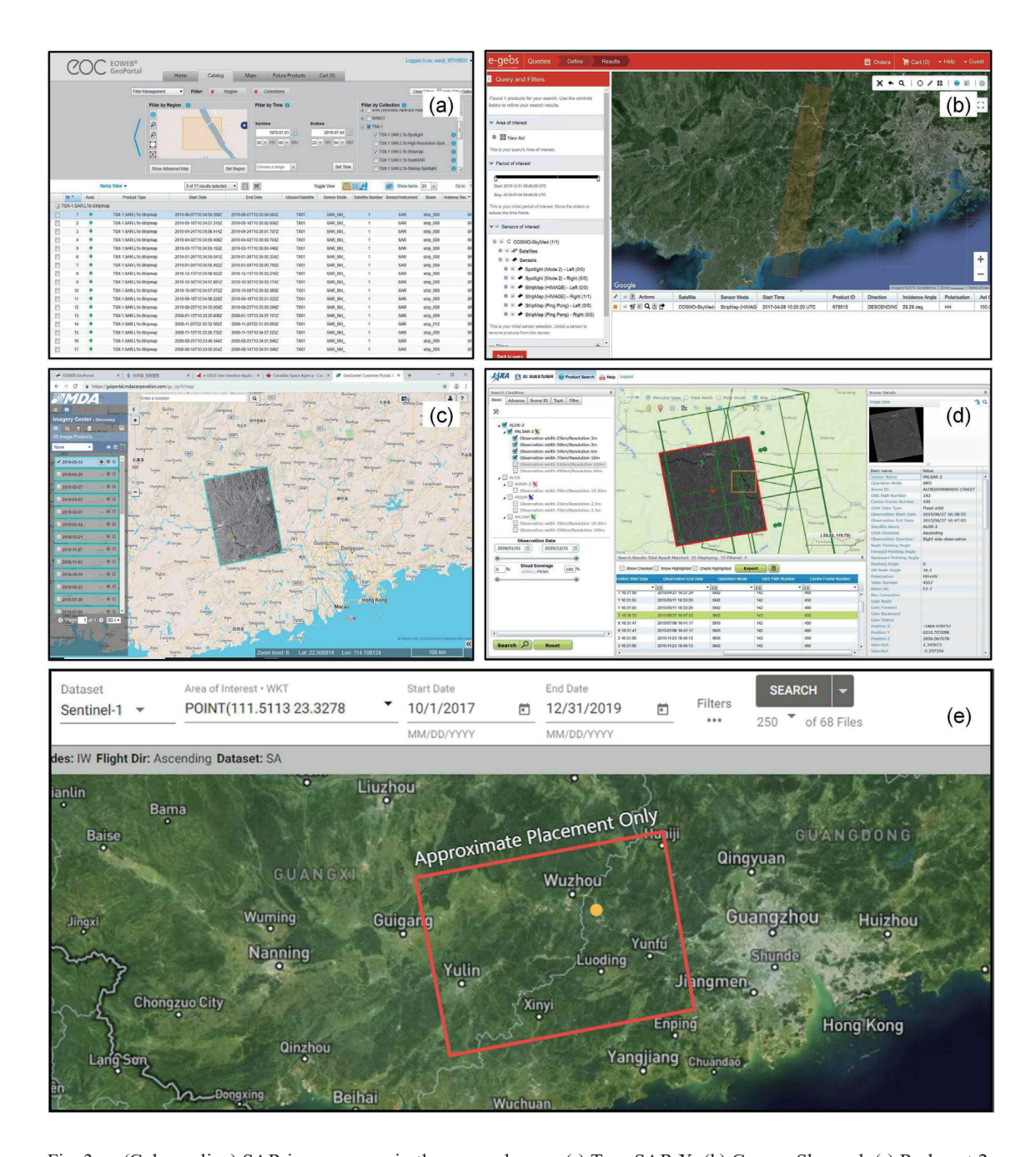


Fig. 3. (Color online) SAR image query in the research area. (a) TerraSAR-X. (b) Cosmo-Skymed. (c) Radarsat-2. (d) ALOS-2 PARSAR2. (e) Sentinel-1A.

spatial resolution of 2.3 × 13.9 m² for Single-Look Complex (SLC) images in the Interferometric Wide mode. The open access strategy employed by Sentinel-1A/B renders it the most comprehensive global coverage and the largest repository of Synthetic Aperture Radar (SAR) satellite data available. In response to the research inquiry, our study area encompasses 69 scenes of Sentinel-1A Ascending images from October 7, 2017 to January 1, 2020, with a maximum time interval of 12 days, as illustrated in Fig. 3. The radar coverage effect provided by

Radarsat-2 platform data is also deemed relatively ideal within the study area. From April 2017 to May 2019, a total of 27 Ascending image scenes were covered at an average rate of one scene per month, as depicted in Fig. 3. However, owing to its commercial nature and high cost (market price ranging between ¥18k and ¥23k/scene), Radarsat-2 data was not considered for this monitoring work, given its lower time resolution than that offered by Sentinel-1A, along with coherence considerations. The Advanced Land Observing Satellite-2 (ALOS-2), launched by the Japan Aerospace Exploration Agency in January 2014, offers range resolutions around 4.3 m and azimuth resolutions around 3.2 m when operating under ScanSAR Multi-look imaging mode conditions. Following consultation, our work area encompasses a total of 11 ascending image scenes captured between June 27, 2015 and April 27, 2019, with a maximum time interval of up to 350 days. Although ALOS-2 data is not currently accessible through open access channels, its high-resolution imaging characteristics, coupled with the advantages associated with L-band (~23.6 cm) long deformation gradient monitoring ability, make it an ideal data source for this work

In summary, Sentinel-1A and ALOS-2 PARSAR2 are proposed to be used as data sources for highway slope monitoring in this work. Table 1 shows a list of SAR data parameters employed in the analysis. It is crucial to highlight that both datasets utilized in this monitoring endeavor consist of Ascending data. While the imaging geometry remains consistent, variations in spatiotemporal resolutions inevitably lead to different monitoring outcomes. Through a detailed analysis of the monitoring results, we can delve into the potential applications of SAR satellites in the context of small highway slope monitoring. Furthermore, to simulate and mitigate terrain phase interference, Shuttle Radar Topography Mission (SRTM) Digital Elevation Model (DEM) data with a resolution of 30 m is incorporated in this work.

3. Methodology

3.1 D-InSAR processing

The data product provided by the SAR satellite platform is the SLC image, which contains amplitude and phase information. The phase information serves the purpose of gauging the distance between the observed target and the sensor, while the deformation is the distance change between two images obtained at different time intervals. As such, the bedrock of all

Table 1 SAR data parameters.

Sensor	ALOS-2	Sentinel-1A
Orbit number	11	69
Orbit direction	Ascending	Ascending
Heading angle (°)	349.8	347.6
Look angle (°)	40.55	41.78
Pixel spacing (m; range × azimuth)	4.3×3.2	2.3×13.9
Timespan	27/6/2015-27/4/2019	7/10/2017–1/1/2020
Number of scenes	11	69

multi-temporal InSAR techniques involves interferometry processing applied to pairs of SAR images from repeated orbits, aimed at recovering deformation phase information. However, there are spatial and temporal differences in SAR images from repeated orbits. The interferometric phase at each point in the image pairs also contains elevation information and random noise specific to that point, introducing interference with the deformation phase and hindering the extraction of accurate deformation. To mitigate these challenges, we employed the image co-registration program from the GAMMA software package, facilitating the co-registration of SLC images with a reference image. This step eliminates the impact of geometric deviations between images on the interferometric phase. Owing to the significant difference between the range and azimuth resolutions of the Sentinel-1A image, conventional 4:1 or 5:1 multi-look processing is typically adopted in interferometry processing. However, recognizing the small geometric size of the highway slope and the imperative to preserve details, we chose not to subject Sentinel-1A and ALOS-2 data to multi-look processing during Differential Interferometry Synthetic Aperture Radar (D-InSAR) processing.

To mitigate the impact of elevation information on the interferometric phase, we utilized 30-m-resolution SRTM DEM data to simulate the interferometric phase. This simulation is based on the spatial baseline of the image pairs. The DEM is geocoded into the radar coordinate system of the SAR image using the geocoding command in GAMMA software. This process effectively eliminates terrain-induced phase contributions from the interferometric phase. The noise component in the interferogram typically exhibits random characteristics, and its effect can be effectively suppressed through the application of a filtering method. To preserve desirable deformation edge characteristics, we employed a nonlocal filtering approach with a half-window size set at 4 for filtering differential interferometric phases. (23) The resulting interferometric phase, obtained through D-InSAR processing, can be decomposed into multiple components:

$$\emptyset = \emptyset_{topo} + \emptyset_{def} + \emptyset_{atm} + \emptyset_{noise},$$
 (1)

where \emptyset_{topo} represents the DEM residual phase, \emptyset_{def} is the deformation phase, and \emptyset_{atm} is the atmospheric phase. In addition, the interference phase also incorporates the random noise phase \emptyset_{noise} . To assess the interferogram's quality, coherence coefficients were estimated using window sizes of 32×32 for Sentinel-1A and 16×16 for ALOS-2. (24) Subsequently, a threshold of an average coherence value at 0.25 was applied to select coherent point targets. As depicted in Eq. (1), a single interferogram alone cannot accurately extract deformation information. Consequently, many researchers have proposed Multi-Temporal InSAR technology (MT-InSAR) to effectively mitigate spatiotemporal decorrelation, DEM errors, and atmospheric effects in the D-InSAR processing. Representative methods include Persistent Scatterer InSAR (PS-InSAR)(25,26) and Small Baseline Subset InSAR (SBAS-InSAR). These MT-InSAR technologies form small baseline sets based on multiple interferograms and construct deformation models from the time series to estimate deformation parameters. Considering the effects of the wavelength and spatial baseline of SLC data on the interference phase, we selected 24d, 700d and 200 m, 300 m as the spatiotemporal baseline thresholds of Sentinel-1A and ALOS-2 data, respectively. Figure 4 shows the spatiotemporal baseline of the interferogram.

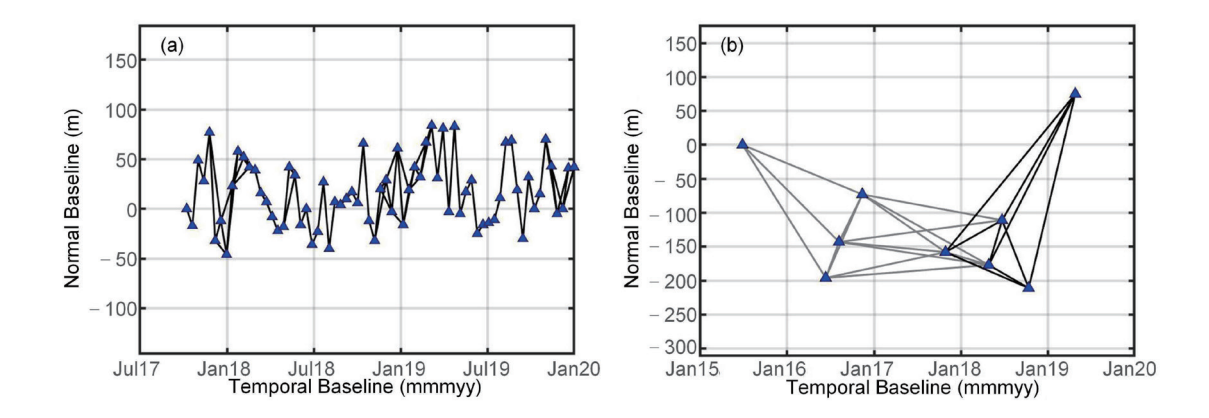


Fig. 4. (Color online) InSAR image pairs. (a) Sentinel-1A. (b) ALOS-2. The image pairs shown by the black line will be used for multi-temporal InSAR processing.

3.2 TCP-InSAR

The PS-InSAR technology proposed by Ferretti *et al.*^(25,26) focuses on identifying permanent scatterers that exhibit relative stability in time series, enabling the reliable detection of subtle deformation characteristics for artificial structures such as cities, bridges, and dams. However, the study area is situated in the hilly region of western Guangdong where dense vegetation poses challenges in selecting a sufficient number of PS points using PS-InSAR technology. In contrast, Berardino *et al.*'s SBAS-InSAR method,⁽²⁷⁾ proposed in 2002, targets pixels that display stable characteristics within short baseline sets. This approach effectively addresses the limitation of monitoring points posed by the PS-InSAR method. Nevertheless, the study area's vegetation and steep terrain introduce unwrapping errors that cannot be overlooked.

In 2010, Zhang *et al.* introduced Temporarily Coherent Points InSAR (TCP-InSAR), a novel approach that integrates the strengths of PS-InSAR and SBAS-InSAR.^(28,29) In the context of interferogram combination, the TCP-InSAR method aligns with the SBAS-InSAR approach, employing a combination strategy that involves multiple main images and short spatiotemporal baselines.^(28,29) We assume the presence of j SAR images within the study period and select an i interferogram based on a specified spatiotemporal baseline threshold. Let us denote the deformation velocity of the TCP point in the i interferogram as v. The deformation phase relative to the reference image can be expressed as

$$\emptyset_{def,l,m}^{i} = -\frac{4\pi}{\lambda} \Delta r_{l,m}^{i} = \sum_{k=1}^{C_{i}-1} (t_{k} - t_{k-1}) v_{k} = \beta_{i} v,$$
(2)

where (l, m) represents the pixel coordinates of a given TCP point, $r_{l,m}^i$ denotes the distance between the pixel and the sensor, λ represents the radar wavelength associated with the SAR sensor platform, and the coefficient β_i of the deformation rate is linked to the combination mode T_i of the interference pair time baseline.

$$T_i = \begin{bmatrix} t_1 - t_0 & t_2 - t_1 & t_k - t_{k-1} & t_j - t_{j-1} \end{bmatrix}$$
 (3)

Given the positive correlation between the terrain residual phase and the image pair to the spatial baseline in Eq. (1), the expression for the terrain residual phase is

$$\varnothing_{topo,l,m}^{i} = -\frac{4\pi}{\lambda} \frac{B_{\perp}^{i}}{r_{l,m}^{i} \sin \theta^{i}} \Delta h_{l,m} = \alpha_{l,m}^{i} \Delta h_{l,m}, \tag{4}$$

where B_{\perp}^{i} represents the spatial baseline of the interference pair and θ^{i} denotes the local incident angle.

In contrast to the SBAS-InSAR method, which necessitates phase unwrapping, TCP-InSAR utilizes the arc formed by adjacent TCP point targets for observation. The phase difference between adjacent TCP points can be expressed as

$$\Delta \varnothing_{l,m,l',m'}^i = \alpha_{l,m}^i \Delta h_{l,m,l',m'} + \beta_i \Delta v + w_{l,m,l',m'}^i. \tag{5}$$

Given the strong spatial correlation of atmospheric delay, the atmospheric phase between adjacent TCP points can be disregarded after separation by difference. The random noise, denoted as $w_{l,m,l',m'}^i$, following the difference operation, adheres to the statistical property of having a mathematical expectation of 0. For the short arc without phase ambiguity, its representation in the time series is

$$\Delta \varnothing = A \begin{bmatrix} \Delta h_{l,m,l',m'} \\ \Delta v \end{bmatrix} + w, \tag{6}$$

where $\Delta\varnothing = \left[\Delta\varnothing_{l,m,l',m'}^1 \quad \Delta\varnothing_{l,m,l',m'}^2 \quad \dots \quad \Delta\varnothing_{l,m,l',m'}^i\right]$ represents the phase difference vector of adjacent TCP points and $A = \left[\alpha \quad \beta\right]$ is the coefficient combination matrix of deformation parameters and DEM residual. Here, $\alpha = \left[\alpha_{l,m}^1 \quad \alpha_{l,m}^2 \quad \dots \quad \alpha_{l,m}^i\right]^T$ and $\beta = \left[\beta_1 \quad \beta_2 \quad \beta_i\right]^T$. Employing the least square method facilitates the resolution of parameters related to Δ h and Δ v in Eq. (6). Subsequent to forming adjacent TCP points into arcs through the outlined steps for parameter estimation, the reliability of the solution can be enhanced by screening effective arcs using a predefined phase threshold. The Delaunay triangulation, eventually constituting the observation of the interference graph, undergoes a secondary parameter estimation. Ultimately, the deformation velocity and DEM residual of each TCP point are obtained by integrating the parameter estimation results relative to the reference point. The processing flow of the TCP-InSAR method is illustrated in Fig. 5.

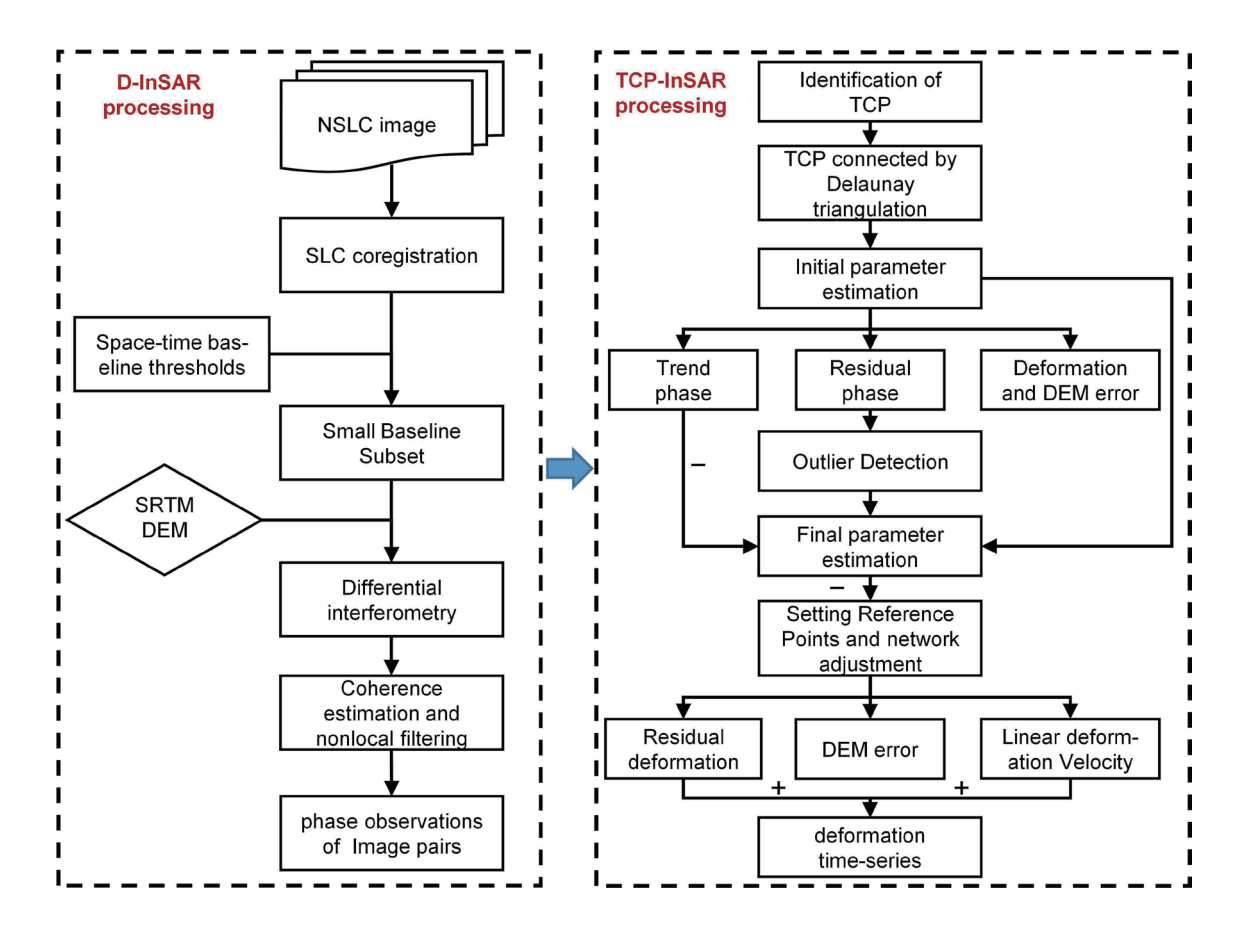


Fig. 5. (Color online) Processing flow of TCP-InSAR method.

4. Results and Discussion

4.1 D-InSAR results

To obtain the interferometric phase, we performed D-InSAR processing separately based on the spatio-temporal baselines of the Sentinel-1 and ALOS-2 datasets. Figure 6 shows the D-InSAR results obtained using the Sentinel-1A images. Given the relatively small size of the slope in relation to the limited resolution of the data, multi-look processing was omitted from the Sentinel-1A images during D-InSAR processing. The analysis of the monitoring results revealed a scarcity of available monitoring points on the slope owing to the low resolution of Sentinel-1A images. Furthermore, the weak noise suppression capability and poor vegetation penetration of the C-band contribute to a significant reduction in overall coherence. The phase components of coherent points selected on the slope are intricate, presenting challenges in identifying meaningful and consistent deformation information.

In contrast to the C band with a wavelength of approximately 5 cm, the ALOS-2 data in the L band exhibits a longer wavelength of 23.6 cm, enabling effective penetration through low vegetation and substantial enhancement in noise suppression capabilities. Figure 7 shows the D-InSAR results obtained using the ALOS-2 PALSAR images. Observations from Fig. 7 reveal

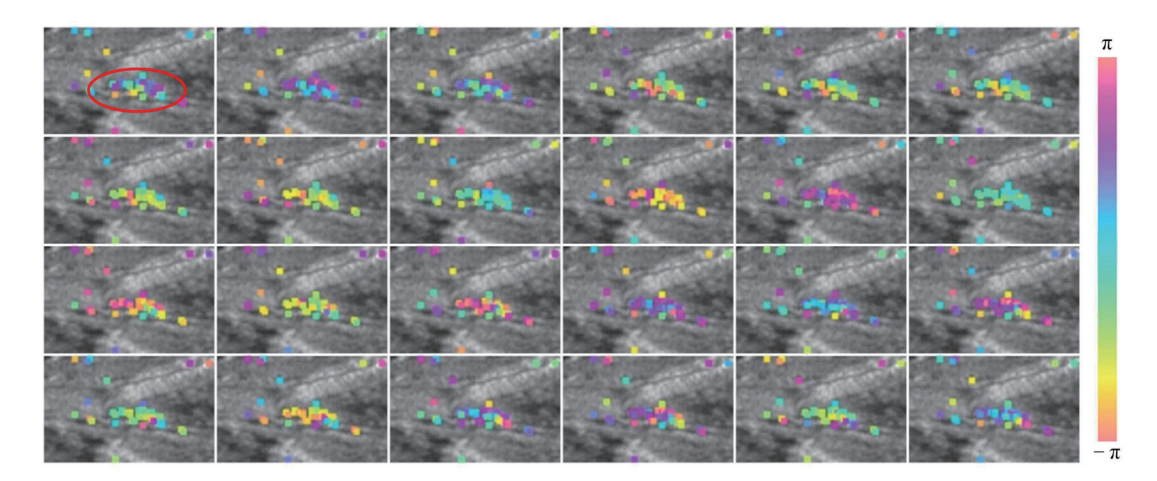


Fig. 6. (Color online) D-InSAR results acquired from Sentinel-1A images. The location of the highway slope is indicated by the red outline.

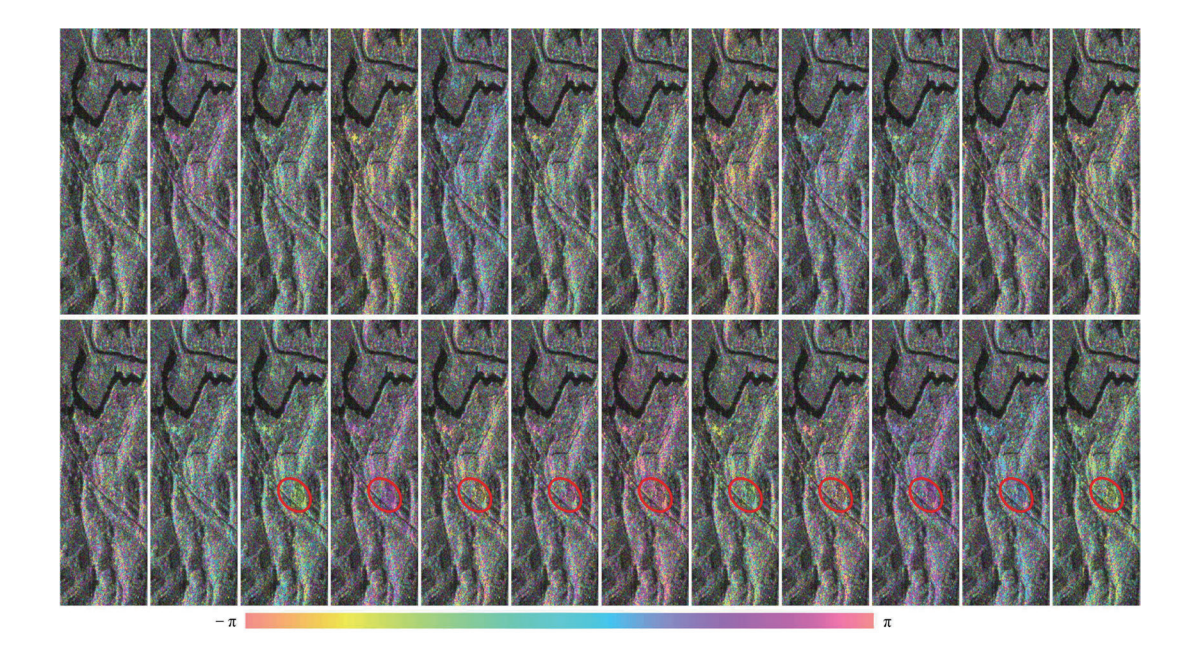


Fig. 7. (Color online) D-InSAR results acquired from ALOS-2 PARSAR2 images. The location of the highway slope is indicated by the red outline. We only drew the red outline in the interferogram after October 28, 2018.

two distinct coherences in different time periods within the ALOS-2 image. The D-InSAR results for the slope before October 28, 2017 exhibit a nearly incoherent feature. Possible explanations for this phenomenon, supported by slope reinforcement records, include the following: (1) the slope underwent reinforcement in 2016, with a change in slope rate from three to five levels (as shown in Fig. 2), resulting in a significant alteration in ground object attributes, impeding interference formation; (2) prior to the completion of the slope treatment project, dense vegetation covered the surroundings, and the long-time interval of the image presented challenges for ALOS-2 to maintain satisfactory coherence around the slope. However, as

depicted in Fig. 7, upon the completion of the slope reinforcement project, the coherence of ALOS2 data around the slope markedly improved. Additionally, discernible deformation signals in the northeast corner of the slope are evident in these interferograms.

Through the analysis of D-InSAR monitoring results, it is evident that Sentinel-1A is constrained by both resolution and coherence limitations, rendering it incapable of extracting effective deformation information. In contrast, ALOS-2 shows the capacity to maintain favorable coherence following slope reinforcement, enabling the detection of pronounced deformation phases in the interferogram. Consequently, our focus shifted exclusively to the time series analysis of ALOS-2 PARSAR2 images captured in five scenes after October 28, 2017, aimed at assessing the stability of the slope post-reinforcement. The black line in Fig. 4(b) represents the small baseline set of TCP-InSAR processing.

To achieve improved results in time series processing, we utilized Small Baseline Subset image pairs for conducting nonlocal filtering operations using a half-window size of 4. Additionally, we employed a mask threshold of 0.25 to eliminate monitoring points with an unsatisfactory interference effect caused by incoherent noise. Notably, the northeast corner of the slope, delineated by the red dotted line in Fig. 8, exhibits conspicuous deformation characteristics. Leveraging the phase information from these image pairs, we conducted TCP-InSAR time series analysis.

4.2 Deformation velocity results

When employing the TCP-InSAR method for parameter estimation, we assumed that the highway experiences no deformation. A high-coherence point on the highway serves as a reference for correcting the deformation estimation results. Figure 9 shows the average deformation velocity of the slope, derived through secondary parameter estimation using the TCP-InSAR method. The analysis of Fig. 9 revealed that the predominant deformation is

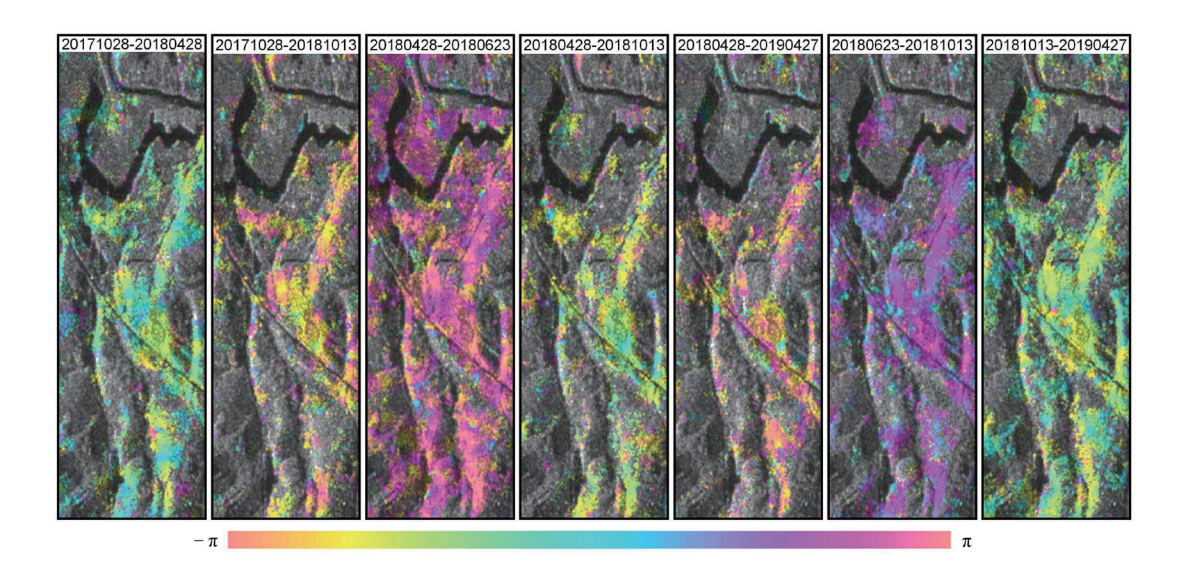


Fig. 8. (Color online) Interference phase following nonlocal filtering.

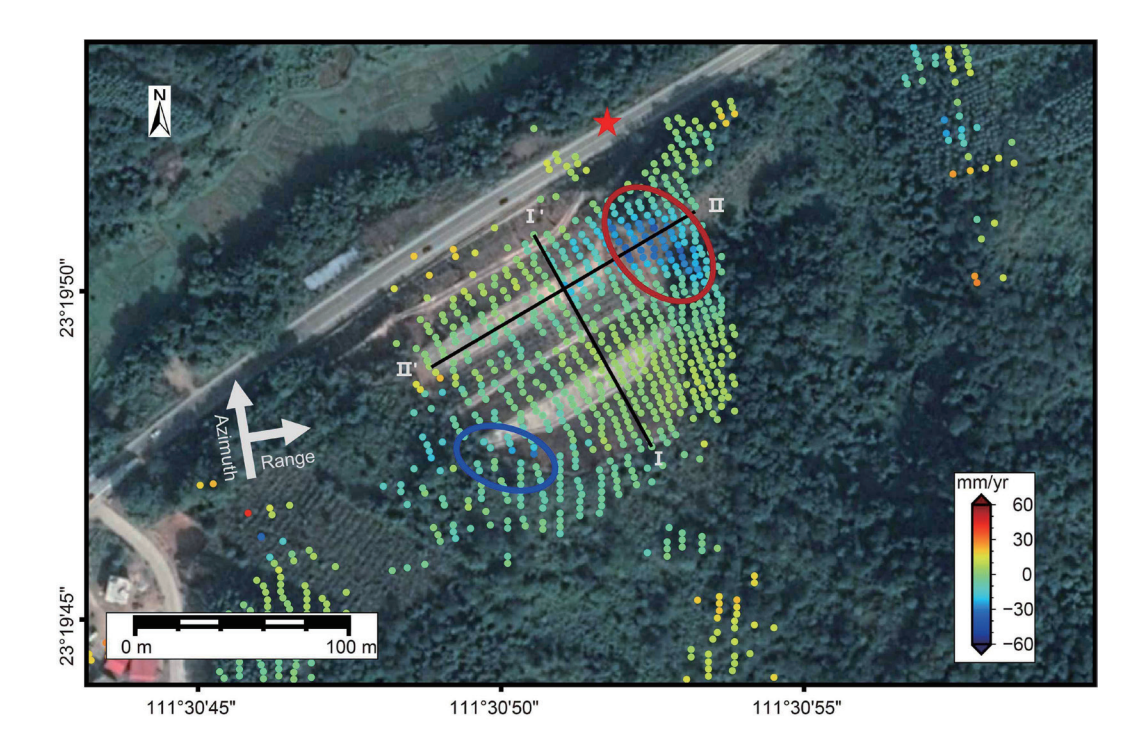


Fig. 9. (Color online) LOS deformation velocity maps of the highway slope. The red and blue outline represents the primary deformation zone of the highway slope. The red asterisks represent the position of the reference point.

concentrated in the northeast corner at the leading edge of the slope, with the maximum deformation velocity along the radar line of sight (LOS) reaching -60 mm/yr. By cross-referencing this observation with the UAV image post-slope reinforcement project [depicted in Fig. 2(b) with a red dotted circle], it is evident that the northeast corner lacks special support measures. Considering the study area's location in South China, characterized by abundant rainfall, especially during the summer with frequent heavy rainfall events, and the absence of specific measures such as retaining wall support and slope water drainage in the northeast corner, it becomes apparent that this area is susceptible to slope slip and soil erosion, providing a plausible explanation for the observed deformation. Furthermore, a distinct deformation signal is evident at the trailing edge of the slope, as highlighted by the blue dotted box in Fig. 9. The inspection of the corresponding UAV image indicates coverage by low vegetation in this region. When coupled with the InSAR results, this area may signify a concealed slip point warranting attention.

To gain a comprehensive understanding of the slope's deformation characteristics, we established a cross section along its direction, denoted as I–I' in Fig. 9. The deformation results along this cross section are illustrated in Fig. 10(a). The analysis of the deformation velocity on the cross section revealed a relatively stable trailing edge with a maximum deformation rate not exceeding –10 mm/yr. Moreover, the field UAV imagery indicated the absence of significant deformations above the third-level berm area. However, upon transitioning from the third-level berm to the third-level slope along this profile, an acceleration in deformation was observed,

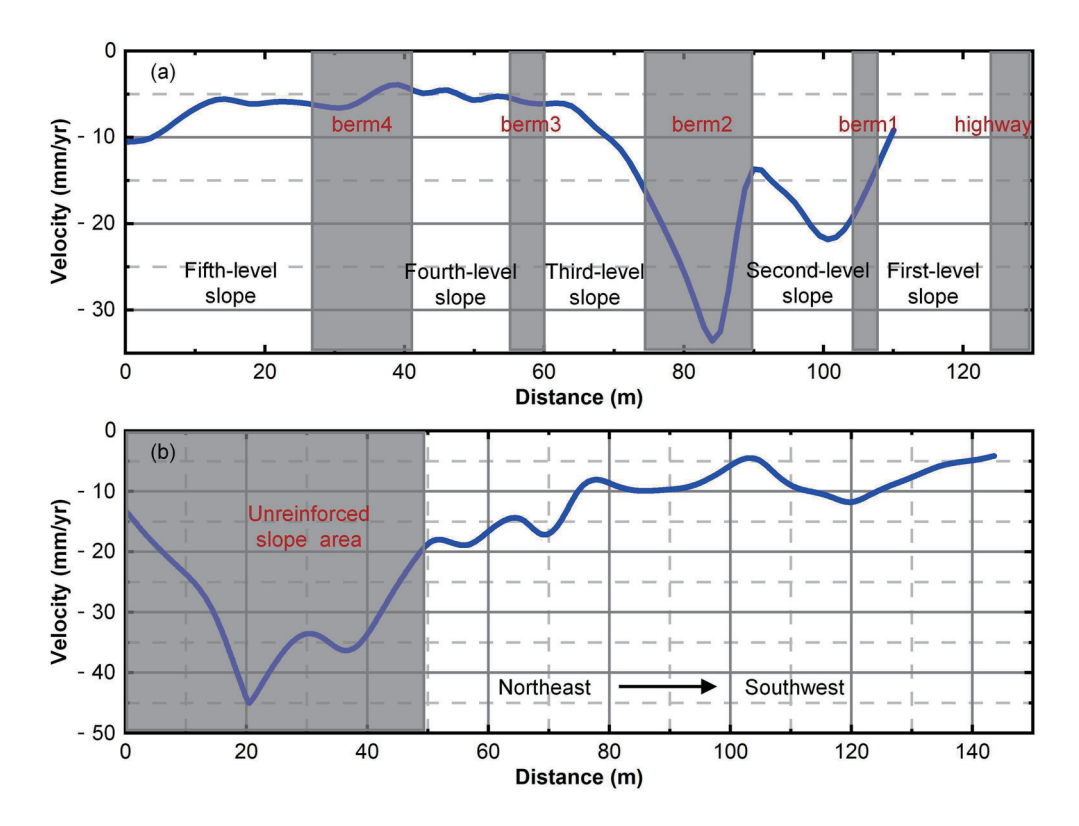


Fig. 10. (Color online) Deformation velocity profiles of highway slope cross sections. (a) Cross section II–II. (b) Cross section II–II.

increasing from -10 to -25 mm/yr. This trend of accelerated deformation extends towards and reaches its peak value at approximately -33 mm/yr in the middle portion of the second-level berm. Field investigation photos in Figs. 11(b) and 11(c) vividly illustrate pronounced deformations within the second-level berm, even showing ground tensile cracking phenomena. In contrast, no obvious crack marks were found on the third-level slopes, consistent with the InSAR monitoring results. A preliminary inference suggests that deformations within the second-level berm pull rearward against the third-level slopes, inducing minor deformations in the latter. As the profile gradually transitions from the second-level berm into the second-level slopes, deformations progressively decelerate until they return below -20 mm/yr. Upon entering the first-level berm along this profile, deformations increase to approximately -23 mm/yr. When the profile transforms into a first-class slope, the supporting effect of the slope footwall effectively mitigates deformation phenomena, resulting in deformation rates below -10 mm/yr.

On the basis of deformation results of the aforementioned cross section, it can be inferred that the deformations observed on the second- and third-level slopes may have been caused by the deformation of the second-level berm. Consequently, we established a perpendicular cross section II–II' along the second-level berm (as shown in Fig. 9) and obtained deformation velocity results as depicted in Fig. 10(b). The analysis of these results revealed a discernible decreasing distribution of deformation velocity from the northeast to the southwest. In the region devoid of reinforcement in the northeast corner of the slope, the deformation velocity peaks at –44 mm/yr.



Fig. 11. (Color online) Photographs of field investigation. (a) Third-level slope. (b) Cracks on secondary berm. (c) Dislocation of the retaining wall top in the secondary berm.

Conversely, the reinforced area situated at the edge of the second-level berm exhibits a reduced deformation velocity of approximately -20 mm/yr, while the southwest corner of the second-level berm records a deformation velocity of -8 mm/yr, indicating a relatively stable deformation pattern. Despite the presence of two incoherent areas in the middle of the second-level berm, they do not significantly impact the overall deformation trend assessment. In summary, the slope's deformation is predominantly attributed to slip traction in the unreinforced area of the northeast corner.

4.3 Time series analysis

To gain a deeper understanding of the slope's deformation characteristics, we decomposed the deformation into a time series. The cumulative deformation map of the slope monitoring is shown in Fig. 12. Taking the first SAR data after slope reinforcement as our reference point, i.e., setting October 28, 2017 as zero deformation, all subsequent deformations were measured relative to this time point. From the results of cumulative deformation analysis, it can be observed that significant southwest corner deformations primarily occurred between October 28, 2017 and April 28, 2018 with a maximum displacement of -60 mm; however, there was no

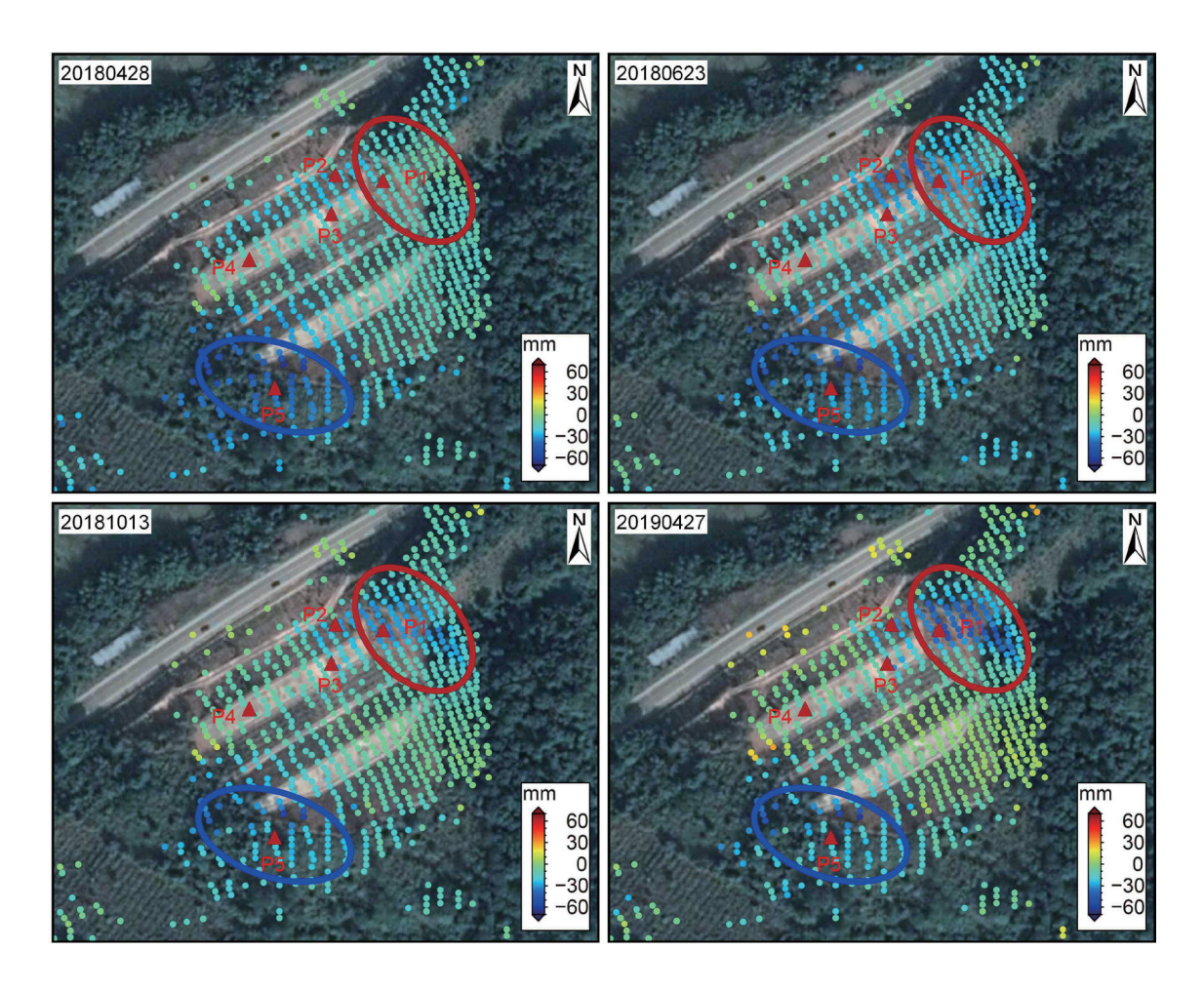


Fig. 12. (Color online) Cumulative deformation maps of the highway slope.

substantial increase in cumulative deformation during the following year. Conversely, deformations at the northeast corner of the slope continued to grow from October 29, 2017 to April 27, 2019 with the maximum displacement also reaching -60 mm.

To gain a deeper understanding of the time characteristics of slope deformation, we selected five key points on the slope for the analysis of their respective deformation time series. These points include the following: (1) the unreinforced area in the northeast corner, denoted as P1, (2) the second berm proximate to the unreinforced area in the northeast corner, denoted as P2, (3) the secondary slope in the vicinity of the unreinforced area, denoted as P3, (4) the southwest corner of the secondary berm, denoted as P4, and (5) the southwest corner edge of the slope, denoted as P5. Figure 13 shows the results of the deformation time series for these five points, each exhibiting varying degrees of deformation signals. Point P1 experienced a minor deformation magnitude with a displacement of -10 mm from October 2017 to April 2018. The rate of deformation began to increase between April and June 2018, resulting in a cumulative displacement reaching -20 mm within two months. Although it is difficult to draw a definitive conclusion without rainfall data, this acceleration may be related to heavy rainfall during

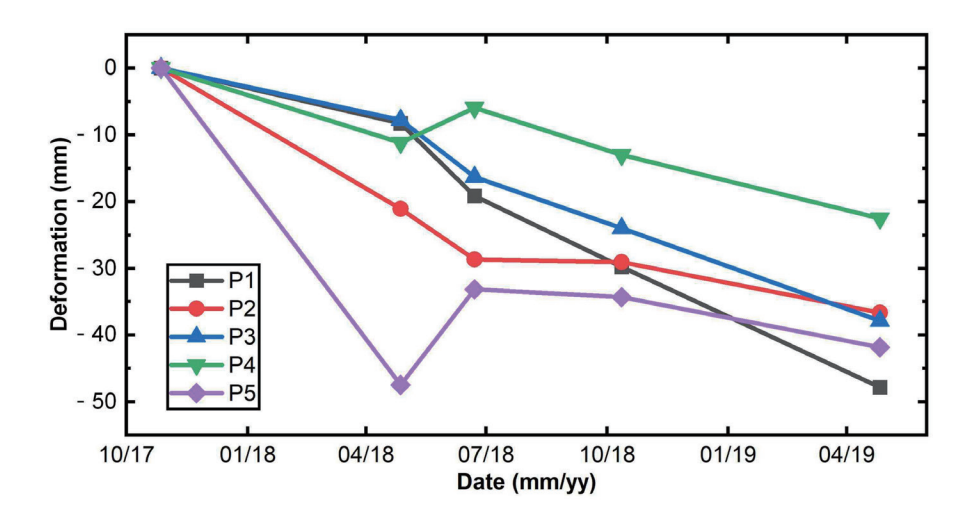


Fig. 13. (Color online) Results of deformation time series for the characteristic points on the slope.

summer. Subsequently, point P1 displayed linear growth in its deformations, accumulating a total displacement of -50 mm by April 2019. Considering the average deformation velocity, cumulative deformation map, and time series data for point P1, we infer that the northeast deformation area remains in a developmental stage, warranting attention from highway management authorities. Point P2 is situated close to an unreinforced section on the secondary berm's slope and exhibits similar trends as observed at point P1. This further confirms that more severe deformations occurring at the northeast corner are associated with slip-induced movements due to a lack of reinforcement. Point P5, situated at the southwest corner of the slope edge, exhibited pronounced deformation from October 2017 to April 2018, peaking at approximately -47 mm. Post-June 2018, a slight rebound occurred, followed by gradual deformation. Between June 2018 and April 2019, the deformation remained under 5 mm. By leveraging the information provided by the cumulative deformation map, it is discernible that the area experiencing deformation on the southwest side of the slope, as depicted in the average deformation rate map, is presently characterized by a state of relative stability.

4.4 Potential of InSAR technology in monitoring highway slopes

The assessment of Sentinel-1A and ALOS-2 PARSAR2 images in monitoring highway slopes revealed certain limitations. Sentinel-1A, constrained by its resolution and wavelength, struggles to extract effective deformation information from the slope. Although ALOS-2 can detect certain deformation details of the slope, there are still several shortcomings in its application for highway slope studies.

First, ALOS-2 has a low temporal resolution and limited availability of SAR data. In this work, we utilized only five scenes of ALOS-2 PALSAR2 images, which not only affects the accuracy of deformation parameter estimation but also fails to capture many time-related deformation details that are crucial for analyzing internal or external factors contributing to

deformations. The interpretation of deformation mechanisms is essential for effective prevention and treatment strategies for highway slopes, which may explain why ALOS-2 PARSAR2 is rarely utilized in highway slope monitoring applications.

Second, there is a lack of suitable descending images available. Similar to many highway slopes monitored in this work, their direction aligns closely with the flight path of SAR satellites. Consequently, this leads to an inability to capture deformation signals along the azimuth direction and potentially missing out on various deformation features on these slopes. Additionally, with only one orbit image available, it is possible to obtain only the projection of deformation upward in the LOS, and it becomes challenging to comprehend deformations.

While various factors, such as spatiotemporal resolution, wavelength, and orbit data, have posed limitations on the application of InSAR monitoring for small-scale highway slopes, there is promise on the horizon. The deployment of China's Lutan-1 satellite⁽³¹⁾ and NASA's upcoming launch of the NISAR satellite,⁽³²⁾ both characterized by high spatial resolution and utilizing L-band technology with time resolutions of 8 and 12 days, respectively, brings a sense of excitement to the field. Notably, NISAR will adopt an open access strategy. The synergistic use of these multi-source L-band high-resolution SAR satellites is poised to significantly enhance the application potential of InSAR technology for the precise deformation monitoring of small-scale highway slopes.

In this work, we used ALOS-2 PALSAR2 data to obtain the deformation monitoring results of the study area. However, owing to the limited number of archived SAR images, it is difficult to effectively reveal the potential deformation triggering factors of slopes. In addition, we only used the ascending SAR data, and the LOS deformation will make it difficult to interpret the real deformation scene of the slope. With the accumulation of multi-source L-band high-resolution SAR data, in future studies, we will strengthen the deformation time-series integrating meteorological or environmental datasets (e.g., rainfall and soil moisture), which could help better interpret the observed acceleration in deformation and identify triggering mechanisms. In addition, the improvement of slope deformation recognition ability will provide us with the target area of ground monitoring, so as to strengthen the incorporating ground truth data, such as UAV photogrammetry or GNSS measurements. Finally, with multi-platform SAR fusion, additional insights might be gained through multi-orbit or 3D deformation analysis to better capture complex slope movement patterns.

5. Conclusions

To focus on the deformation monitoring of small-scale highway slopes using InSAR technology, we obtained the deformation monitoring results of the left slope of the Fengkai connecting line K2+500 of Guangkun Expressway based on C-band Sentinel-1A data and L-band ALOS-2 PALSAR2 data. However, owing to the geometric size of the slope and the limited coherence maintenance capability of the C-band, extracting effective deformation phases proved challenging with medium-resolution Sentinel-1A images. Consequently, we employed the TCP-InSAR method for highway slope monitoring based on a dataset comprising five ALOS-2 PALSAR2 images. Despite the constraints of limited SAR data, the high spatial

resolution and data advantages of the L-band enabled us to derive deformation results for the slope spanning from October 2017 to April 2019. Subsequently, we conducted a spatiotemporal feature analysis, leading to the following conclusions:

- (1) Throughout the InSAR observation period, two primary deformation zones were identified on the slope, situated at the northeast corner and the southwest rear edge. The maximum velocity of deformation approaches -60 mm/yr.
- (2) The deformation zone in the northeastern corner is primarily attributed to the uncontrolled slope slip in that area. Cumulative deformation and time-series analyses indicate that the deformation is still in a developmental stage and therefore warrants attention from the highway management department.
- (3) The deformation area in the southwest corner is situated along the lateral trailing edge of the slope. Despite a maximum deformation rate reaching -50 mm/yr, cumulative deformation and time series analysis revealed that the deformation area underwent a significant acceleration only between October 28, 2017 and April 27, 2018, after which it stabilized. The limited time resolution of the ALOS-2 PARSAR2 image prevented a detailed examination of the characteristics of this deformation time series. Therefore, we recommend an on-site investigation by the highway management department for a more comprehensive understanding.
- (4) The second berm of the treated slope exhibits significant deformation, possibly influenced by the slip of the unreinforced slope in the northeast corner. This deformation extends to the second- and third-level slopes connected to it, resulting in minor deformations in these adjacent areas.

The low-temporal-resolution ALOS-2 PARSAR2 image was utilized in this work to monitor the deformation characteristics of the slope, yielding some positive results. With regards to the forthcoming Lutan-1 and NISAR data, we anticipate that leveraging InSAR technology for the precise deformation monitoring of small highway slopes holds significant potential for application.

Author Contributions

Conceptualization, G. L. and W. Z.; methodology, M. L. and W. Z.; investigation, G. L. and L. Z.; writing—original draft preparation, G. L. and W. Z.; writing—review and editing, G. L. and X. C.; Supervision, C. M. and T. L. All authors have read and agreed to the published version of the manuscript.

Funding

This research was supported by the Research Foundation of Education Bureau of Hunan Province, China (Nos. 23C0295 and 24B0701), the Nature Science Foundation of Hunan Province, China (Nos. 2024JJ6411 and 2025JJ70199), the Hunan Provincial Social Science Achievement Review Committee Project (No. XSP22YBC080), and the Nature Science Foundation of Shaoyang City (No. 2024PT6099).

Data Availability Statement

Data sharing not applicable.

Conflicts of Interest

The authors declare no conflict of interest.

References

- D. Huang, Z. A. Wei, Y. L. Chen, and I. Muhammad: Sains Malays. 46 (2017) 2035. https://doi.org/10.17576/jsm-2017-4611-03
- 2 B. Tong, J. J. Guo, and S. Fang: J. Manage. Eng. 37 (2021) 10. https://doi.org/10.1061/(asce)me.1943-5479.0000890
- 3 Y. Q. He, B. Li, and X. Du: Sustainability 15 (2023) 14. https://doi.org/10.3390/su15021287
- 4 H. B. Yu, C. D. Li, J. Q. Zhou, W. Q. Chen, J. J. Long, X. T. Wang, and T. Peng: Landslides 17 (2020) 2619. https://doi.org/10.1007/s10346-020-01468-6
- 5 A. K. L. Kwong, M. Wang, C. F. Lee, and K. T. Law: Eng. Geol. 76 (2004) 27. https://doi.org/10.1016/j.enggeo.2004.06.004
- 6 C. N. Liu, J. J. Dong, C. J. Chen, and W. F. Lee: Landslides 9 (2012) 239. https://doi.org/10.1007/s10346-011-0298-0
- 7 Y. Xue, N. S. Chen, R. X. Tang, Z. Y. Yang, M. J. Jiao, T. Wen, Y. K. Wang, and J. M. Jin: Landslides **22** (2025) 1199. https://doi.org/10.1007/s10346-025-02455-5
- 8 D. Q. Xiao, Y. Q. Yu, W. Zhan, Z. Hu, and X. Yan: Laser Eng. 53 (2022) 267.
- 9 J. Y. Yang, C. J. Xu, S. Wang, and X. H. Wang: J. Geodyn. **135** (2020) 11. https://doi.org/10.1016/j.jog.2020.101707
- 10 M. J. W. Bemelmans, J. Biggs, M. Poland, J. Wookey, S. K. Ebmeier, A. K. Diefenbach, and D. Syahbana: J. Geophys. Res.-Solid Earth 128 (2023) 27. https://doi.org/10.1029/2022jb025669
- X. F. Zhang, M. Feng, J. H. Xu, D. Z. Yan, J. Wang, X. Q. Zhou, T. Li, and X. Zhang: Int. J. Digit. Earth. 16 (2023) 3923. https://doi.org/10.1080/17538947.2023.2260778
- 12 G. S. Liu, J. Hu, L. L. Liu, Q. Sun, and W. Q. Wu: Remote Sens. 15 (2023) 22. https://doi.org/10.3390/rs15164110
- 13 L. Emadali, M. Motagh, and M. H. Haghighi: Eng. Struct. 143 (2017) 261. https://doi.org/10.1016/j.engstruct.2017.04.009
- 14 G. S. Liu, B. Wang, Q. Sun, J. Hu, L. L. Liu, W. J. Zheng, and L. Y. Zou: IEEE J. Sel. Top. Appl. Earth Observ. Remote Sens. 18 (2025) 2908. https://doi.org/10.1109/jstars.2024.3523294
- 15 W. J. Zheng, J. Hu, Z. Lu, X. Hu, Q. Sun, J. H. Liu, J. J. Zhu, and Z. W. Li: J. Geophys. Res.-Solid Earth 128 (2023) 21. https://doi.org/10.1029/2022jb026232
- 16 X. G. Shi, X. Hu, N. Sitar, R. Kayen, S. W. Qi, H. J. Jiang, X. D. Wang, and L. Zhang: Remote Sens. Environ. **265** (2021) 9. https://doi.org/10.1016/j.rse.2021.112664
- W. Y. Gong, M. M. Darrow, F. J. Meyer, and R. P. Daanen: Remote Sens. Environ. 221 (2019) 722. https://doi.org/10.1016/j.rse.2018.12.014
- 18 X. J. Su, Y. Zhang, X. M. Meng, D. X. Yue, J. H. Ma, F. Y. Guo, Z. Q. Zhou, M. U. Rehman, Z. Khalid, G. Chen, R. Q. Zeng, and F. M. Zhao: J. Mountain Sci. 18 (2021) 2540. https://doi.org/10.1007/s11629-021-6686-6
- 19 L. L. Zhang, K. R. Dai, J. Deng, D. Q. Ge, R. B. Liang, W. L. Li, and Q. Xu: Remote Sens. 13 (2021) 14. https://doi.org/10.3390/rs13183662
- 20 M. Zocchi, A. K. Kasaragod, A. Jenkins, C. Cook, R. Dobson, T. Oommen, D. Van Huis, B. Taylor, C. Brooks, R. Marini, F. Troiani, and P. Mazzanti: Remote Sens. 15 (2023) 22. https://doi.org/10.3390/rs15123016
- 21 S. C. Zhang, Q. Y. Fan, Y. F. Niu, S. C. Qiu, J. Z. Si, Y. H. Feng, S. Q. Zhang, Z. W. Song, and Z. H. Li: Landslides **20** (2023) 447. https://doi.org/10.1007/s10346-022-01979-4
- 22 A. J. Yao, Y. F. Gong, Y. L. Li, T. Tian, and C. S. Xu: J. Test. Eval. **50** (2022) 1906. https://doi.org/10.1520/jte20210423
- 23 Y. D. Gao, S. B. Zhang, T. Li, L. Guo, Q. F. Chen, and S. J. Li: Opt. Lasers Eng. **121** (2019) 1. https://doi.org/10.1016/j.optlaseng.2019.03.008
- 24 O. Mora, J. J. Mallorqui, and A. Broquetas: IEEE Trans. Geosci. Remote Sens. 41 (2003) 2243. https://doi.org/10.1109/tgrs.2003.814657

- 25 A. Ferretti, C. Prati, and F. Rocca: IEEE Trans. Geosci. Remote Sens. 38 (2000) 2202. https://doi.org/10.1109/36.868878
- 26 A. Ferretti, C. Prati, and F. Rocca: IEEE Trans. Geosci. Remote Sens. 39 (2001) 8. https://doi.org/10.1109/36.898661
- 27 P. Berardino, G. Fornaro, R. Lanari, and E. Sansosti: IEEE Trans. Geosci. Remote Sens. 40 (2002) 2375. https://doi.org/10.1109/tgrs.2002.803792
- 28 L. Zhang, X. L. Ding, and Z. Lu: ISPRS-J. Photogramm. Remote Sens. 66 (2011) 146. https://doi.org/10.1016/j.isprsjprs.2010.10.004
- 29 L. Zhang, X. L. Ding, and Z. Lu: IEEE Trans. Geosci. Remote Sens. 49 (2011) 547. https://doi.org/10.1109/tgrs.2010.2052625
- 30 Z. W. Li, X. L. Ding, C. Huang, G. Wadge, and D. W. Zheng: J. Atmos. Sol.-Terr. Phys. 68 (2006) 1189. https://doi.org/10.1016/j.jastp.2006.03.002
- 31 Y. N. Ji, X. Zhang, T. Li, H. D. Fan, Y. Z. Xu, P. Z. Li, and Z. M. Tian: Remote Sens. **15** (2023) 21. https://doi.org/10.3390/rs15245668
- 32 X. D. Huang, M. Reba, A. Coffin, B. R. K. Runkle, Y. B. Huang, B. Chapman, B. Ziniti, S. Skakun, S. Kraatz, P. Siqueira, and N. Torbick: Remote Sens. Environ. 253 (2021) 14. https://doi.org/10.1016/j.rse.2020.112180